Friedel oscillations and chiral superconductivity in monolayer NbSe₂

Julian Siegl, ^{1,*} Anton Bleibaum, ¹ Wen Wan, ² Marcin Kurpas, ³ John Schliemann, ¹ Miguel M. Ugeda, ^{2,4,5} Magdalena Marganska, ¹ and Milena Grifoni^{1,†}

¹Institute for Theoretical Physics, University of Regensburg, 93 053 Regensburg, Germany
²Donostia International Physics Center, Paseo Manuel de Lardizábal 4, 20018 San Sebastián, Spain.
³Institute of Physics, University of Silesia in Katowice, 41-500 Chorzów, Poland
⁴Centro de Física de Materiales, Paseo Manuel de Lardizábal 5, 20018 San Sebastián, Spain.
⁵Ikerbasque, Basque Foundation for Science, Bilbao 48013, Spain
(Dated: December 3, 2024)

In 1965 Kohn and Luttinger proposed a genuine electronic mechanism for superconductivity. Despite the bare electrostatic interaction between two electrons being repulsive, in a metal electron-hole fluctuations can give rise to Friedel oscillations of the screened Coulomb potential. Cooper pairing among the electrons then emerges when taking advantage of the attractive regions. The nature of the leading pairing mechanism in some two-dimensional transition metal dichalcogenides is still debated. Focusing on NbSe₂, we show that superconductivity can be induced by the Coulomb interaction when accounting for screening effects on the trigonal lattice with multiple orbitals. Using ab initio-based tight-binding parametrizations for the relevant low-energy d-bands, we evaluate the screened interaction microscopically, in a scheme that includes Bloch overlaps and Umklapp processes. In the direct space, we find long-range Friedel oscillations which alternate in sign. The momentum-resolved gap equations predict two quasi-degenerate nematic solutions near the critical temperature T_c , signaling the unconventional nature of the pairing. Their complex linear combination, i.e., a chiral gap with p-like symmetry, provides the ground state of the system. Our prediction of a fully gapped chiral phase well below T_c is in agreement with the spectral function extracted from tunneling spectroscopy measurements of single-layer NbSe₂.

In conventional superconductors, electron pairing arises from virtual phonon exchange [1]. In this case, the slowly moving ions mediate an effective attractive interaction that allows the electrons to overcome their mutual repulsion and form Cooper pairs. This mechanism favors s-wave pairing, where the total spin of the electron-pair is zero, and the gap function is isotropic in momentum space. Kohn and Luttinger have proposed an alternative pairing mechanism originating from pure Coulomb repulsion [2]. It is mediated by electron-hole fluctuations of the metal, which result in long-range Friedel oscillations [3] of the screened Coulomb interaction. For conventional superconductors, however, the effect is subleading compared to phonon-induced pairing [2]. As we shall show, it can yield gap sizes compatible with the experiment in the compound investigated in this work, monolayer NbSe₂.

When superconductivity emerges from screened repulsion, the free energy is minimized by an anisotropic gap function [4], and the pairing symmetry is associated to irreducible representations of the crystal. If the symmetry of the Bravais lattice allows a two-dimensional representation, Coulomb repulsion can even mediate a superconducting chiral phase, with spontaneous time-reversal symmetry breaking [5]. Two-dimensional (2D) systems with trigonal lattice are potential candidates for becoming chiral superconductors [6–8]. Evidence for chiral d-wave superconductivity has recently been reported for tin monolayers on a Si(111) surface [9], and a transition

from a nematic to a chiral phase has been proposed for TaS₂ [10–12]. Here we microscopically investigate the nature of superconductivity in monolayer NbSe₂, a 2D compound of the family of transition metal dichalcogenides (TMDs) with Nb atoms arranged on a trigonal lattice. It combines strong Ising spin-orbit coupling (SOC) [13–15] with superconductivity [16–18], leading to a violation of the Pauli limit in strong in-plane magnetic fields [19–24], and an incommensurate charge density wave [20, 25, 26]. While bulk NbSe₂ is commonly assumed to be a conventional phonon-mediated superconductor [27, 28], the mechanism for the monolayer limit is still actively discussed and ranges from phonon-mediated [29, 30] to more exotic pairings [23, 31–33]. Our findings, based on a microscopic calculation of the screened interaction, support the unconventional nature of the superconductivity in the monolayer case.

The expected enhanced importance of unconventional pairing in 2D TMDs arises from their fragmented Fermi surface, cf. Fig. 1, which implies distinct intervalley and intravalley scattering processes, and whose amplitude can be large due to the weaker screening in lower dimensions [34, 35]. Indeed, model calculations have shown that an effective attraction from competing repulsive interactions requires dominance of the short-range intervalley scattering over the long-range intravalley one [23, 32, 36]. In this work, we show that a generalized random phase approximation (RPA) on the trigonal lattice of Nb atoms yields a selectively screened Coulomb interaction, that favors short-range intervalley scattering of Cooper pairs. The multi-orbital character of the valence band, the Umklapp processes as well as the spatial

^{*} Julian.Siegl@ur.de

[†] Milena.Grifoni@ur.de

distribution of the atomic d-orbitals play an important role in this context. In the real space the screened potential exhibits Friedel oscillations with alternating sign, thus providing a realization of the pairing mechanism based on electron-hole fluctuations proposed by Kohn and Luttinger [2]. Upon solving the coupled gap equations for the full screened potential, we find a stable, quasi-degenerate nematic phase near $T_{\rm c}$. As the temperature decreases the system smoothly transitions to a gapped p-wave-like chiral phase. Our predictions are in very good agreement with low-temperature tunneling spectroscopy measurements acquired on monolayer NbSe₂.

Band structure and orbital composition

The starting point for our considerations is a tight-binding model for the Bloch band structure of monolayer NbSe₂ obtained by using the three most relevant orbitals of Nb, $d_{z^2} = d_{2,0}$ and $d_{2,\pm 2} = d_{x^2-y^2} \pm i d_{xy}$ [37], cf. Fig. 1, fitted to ab-initio calculations. Here the parametrization by He et al. [38] is used, but similar results are obtained from the one reported by Kim & Son [39]. There are two metallic valence bands relevant for superconducting pairing at the Fermi level, with distinct spin and which are split by Ising SOC [37]. As seen in the inset of Fig. 1a, multiple disjoint Fermi surfaces are present, which suggests multi-patch superconductivity similar to the one arising in the cuprates and iron pnictides [40, 41]. While the planar d-orbitals mostly contribute to the band composition around the K and K' valleys, $d_{2,0}$ is dominant at the Γ valley, see Fig. 1b.

Screened Coulomb interaction

In crystalline systems the screened interaction is in general a function of both positions of the two interacting charges. It can be expanded as [34]

$$V(\boldsymbol{r}, \boldsymbol{r}') = \frac{1}{\mathcal{V}} \sum_{\boldsymbol{q}', \boldsymbol{G}, \boldsymbol{G}'} V_{\boldsymbol{G}, \boldsymbol{G}'}(\boldsymbol{q}') e^{i(\boldsymbol{q}' + \boldsymbol{G}) \cdot \boldsymbol{r}} e^{-i(\boldsymbol{q}' + \boldsymbol{G}') \cdot \boldsymbol{r}'},$$
(1)

where G, G' are reciprocal lattice vectors, q' is a crystal momentum not confined to lie in-plane, and \mathcal{V} is the sample volume. An exact evaluation of the screened interaction is not possible. However, a closed form can be obtained in the random phase approximation (RPA), in which the polarizability is approximated by that of independent Bloch electrons [34]. With a focus on NbSe₂, we view the orbitals as tightly confined to the plane of the material, cf. Fig. 1. This enables us to obtain a two-dimensional version of the RPA-screened interaction which properly accounts for the long-range behavior. The resulting two-dimensional screened interaction $V_{G,G'}^{2D,RPA}(q)$, cf. the Supplementary Material and Eq.

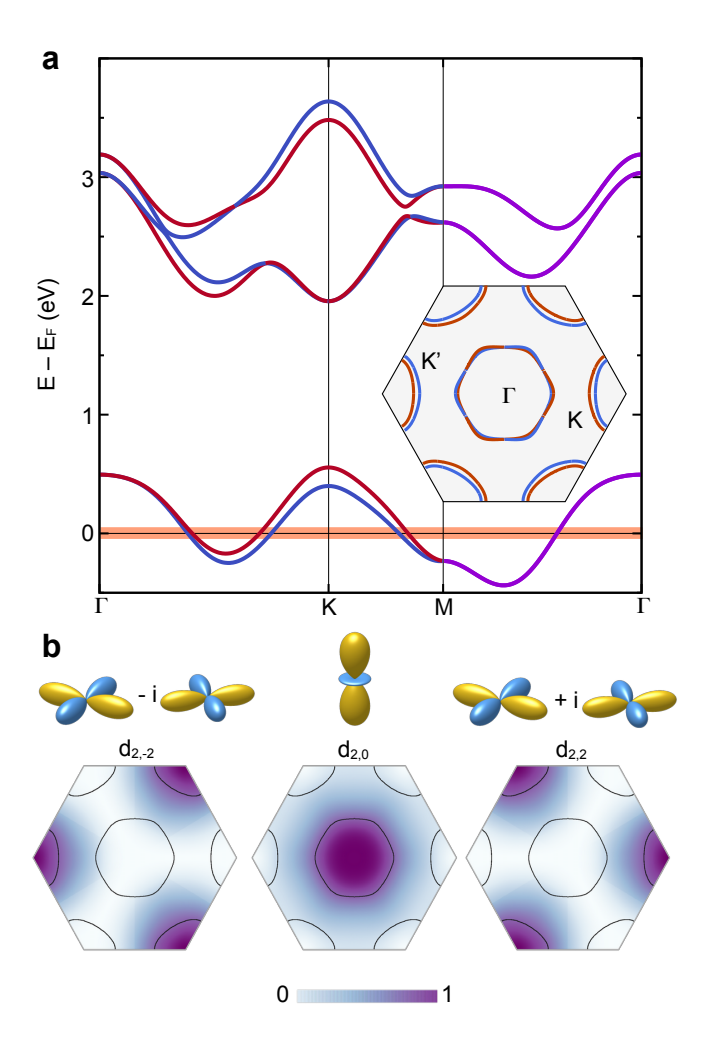


Figure 1. Band structure, Fermi surfaces and orbital contributions in monolayer NbSe₂. a Tight-binding Bloch bands and Fermi surfaces (inset). The Fermi energy lies within the spin split valence bands; the spin degeneracy is removed by the Ising spin-orbit coupling, resulting in spin-resolved Fermi surfaces. b Sketch of the three atomic $d_{l,m}$ orbitals used in the calculation and their contribution to the composition of the valence bands. The quantum numbers l,m denote the total angular momentum of the orbital and its azimuthal projection.

(S.5) therein, can be expressed in terms of the 2D unscreened one, $V_0^{\rm 2D}({\bm q})=\frac{e^2}{2\epsilon_0q},$ as

$$V_{\boldsymbol{G},\boldsymbol{G}'}^{\mathrm{2D,RPA}}(\boldsymbol{q};\omega) = \epsilon_{\boldsymbol{G},\boldsymbol{G}'}^{-1}(\boldsymbol{q};\omega)V_0^{\mathrm{2D}}(\boldsymbol{q}+\boldsymbol{G}'), \quad (2)$$

with $\epsilon_{G,G'}^{-1}$ the inverse of the dielectric tensor

$$\epsilon_{\mathbf{G},\mathbf{G}'}(\mathbf{q};\omega) = \delta_{\mathbf{G},\mathbf{G}'} - V_0^{\text{2D}}(\mathbf{q} + \mathbf{G})P_{\mathbf{G},\mathbf{G}'}(\mathbf{q};\omega).$$
 (3)

The elements of the polarizability tensor in Eq. (3) are given by

$$P_{G,G'}(q;\omega) = \sum_{p,\sigma} \chi_{\sigma}(p+q,p;\omega) \mathcal{F}_{p,p+q}^{\sigma}(G) \mathcal{F}_{p+q,p}^{\sigma}(-G'),$$
(4)

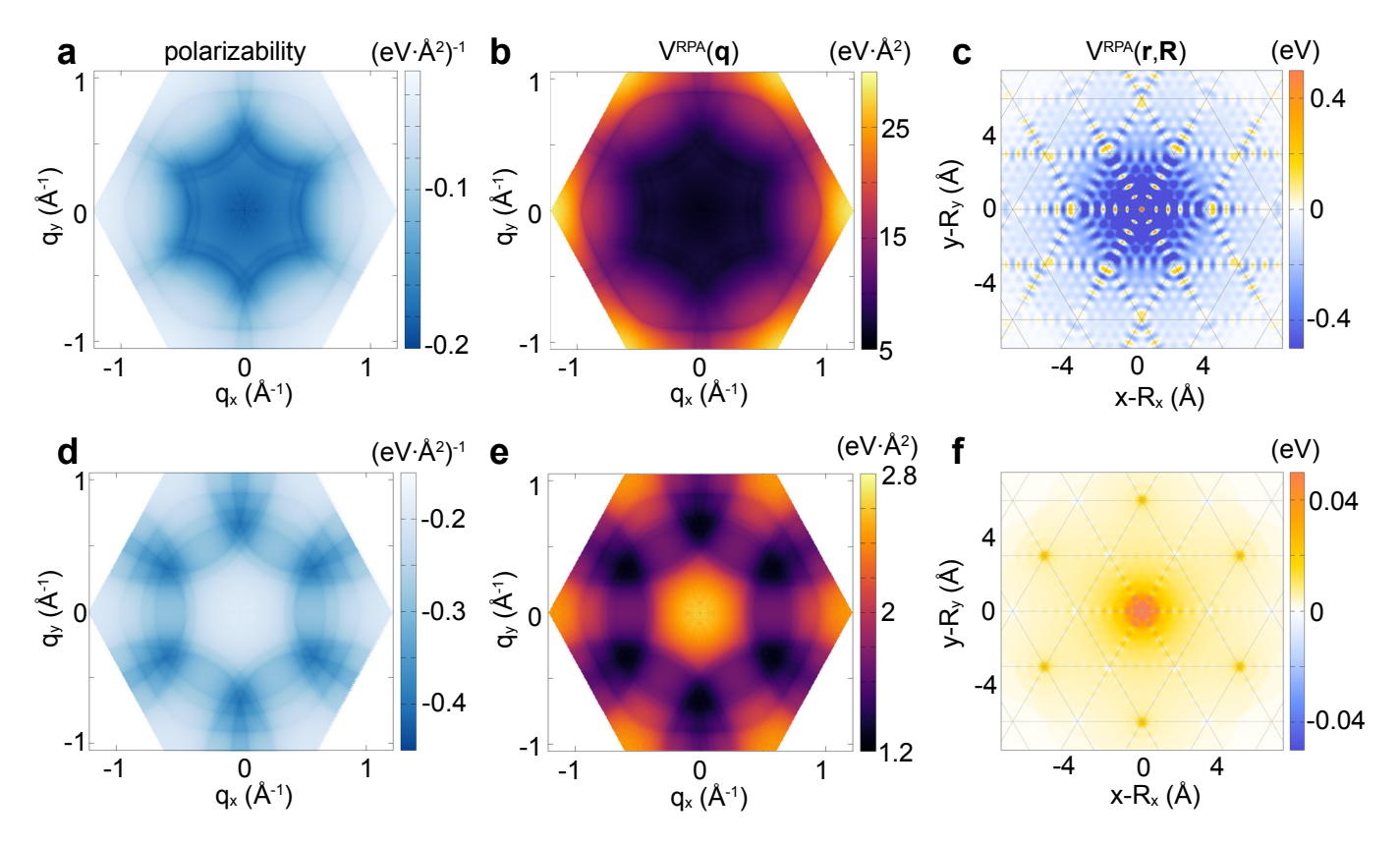


Figure 2. Macroscopic polarizability and screened interaction in the reciprocal and direct space. a The macroscopic polarizability $P_{0,0}$ displays a plateau for small momentum transfers $\mathbf{q} \approx 0$ ($\mathbf{0} =: \mathbf{q}_{\Gamma}$), where its magnitude $|P_{0,0}|$ attains its maximal value, and decreases for large momentum transfers $\mathbf{q} \approx \pm K$ ($K =: \mathbf{q}_K$). This behavior reflects the strong momentum dependence of the Bloch overlaps. b The effective screened interaction is correspondingly strongly suppressed for small momentum transfer and exhibits maxima around $\pm \mathbf{q}_K$. c In real space the screened potential displays Friedel oscillations which bear signatures of the underlying trigonal lattice. The potential is repulsive at the location of the Bravais lattice sites and mostly attractive elsewhere. d,e,f Same observables as in the top panels evaluated in constant matrix element approximation, i.e., setting the Bloch overlaps to 1. In this case, the screening at large momentum transfers is overestimated and hence the screened interaction is largest around \mathbf{q}_{Γ} . In turn, the oscillations in real space are weak and the potential remains repulsive.

with χ_{σ} accounting for electron-hole fluctuations, cf. Eq. (9), and the Bloch overlaps \mathcal{F} defined as

$$\mathcal{F}_{\boldsymbol{k},\boldsymbol{k}'}^{\sigma}(\boldsymbol{G}) = \int_{\mathcal{V}_p} d\boldsymbol{r} e^{-i\boldsymbol{G}\cdot\boldsymbol{r}} \boldsymbol{u}_{\sigma,\boldsymbol{k}}^{\dagger}(\boldsymbol{r}) \boldsymbol{u}_{\sigma,\boldsymbol{k}'}(\boldsymbol{r}). \tag{5}$$

Here $u_{\sigma,k}$ are Bloch spinors, i.e., the periodic part of the Bloch functions holding the information about their orbital composition, and \mathcal{V}_p is the volume of the unit cell. We show in Fig. 2a the macroscopic static polarizability, the element $P_{\mathbf{0},\mathbf{0}}(\mathbf{q},0)$ of the polarizability tensor, properly accounting for the Bloch overlaps. In Fig. 2d the same quantity is shown in the constant matrix element approximation [25, 39], where such overlaps are set to unity. In both cases a plateau is observed for small momentum transfers, $q \approx q_{\Gamma}$. However, while the magnitude $|P_{0,0}|$ of the full macroscopic polarizability is maximal there, it is minimal for the approximated one. As such, retaining the directionality of the Bloch overlaps in momentum space, cf. Fig. S.5 in the Supplementary Material, is crucial to correctly account for the long-range behavior of the screened interaction. This

qualitative difference is visualized in Figs. 2b and 2e where we display the effective screened interaction potential $V^{\text{RPA}}(\boldsymbol{q}) := \sum_{\boldsymbol{G},\boldsymbol{G'}} V_{\boldsymbol{G},\boldsymbol{G'}}^{\text{2D,RPA}}(\boldsymbol{q})$ calculated with and without the constant matrix element approximation for the polarizability, respectively (see Methods). The effective RPA interaction potential shown in Fig. 2b is strongly suppressed for $q \approx q_{\Gamma}$, and displays maxima at $\pm q_K$. The strong suppression for low momentum exchanges q supports the scenario of dominant intervalley scattering discussed by Hörhold et al., Roldán et al. [32, 36]. In constant matrix element approximation, the effective interaction potential is in contrast largest at the q_{Γ} plateau, see Fig. 2e, while being in general smaller throughout the whole Brillouin zone. Hence, the impact of screening for large momentum electron-hole fluctuations is overestimated in the constant matrix element approximation. When turning to the real space, we find that $V^{\text{RPA}}(\mathbf{r}, \mathbf{r}')$, calculated according to Eq. (1), displays sizable Friedel oscillations. The interference pattern originates from the superposition of contributions from q_K and $-q_K$ regions and is a signature of the trigonal lattice. As seen in Fig. 2c, the potential as a function of r, with r' = R fixed to an Nb site, exhibits an onsite repulsion at the origin and repulsive regions around farther Bravais lattice sites while it is mostly attractive elsewhere. This behavior is contrasted by the outcome of the constant matrix element approximation, whereby the screened potential stays purely repulsive, see Fig. 2f. This finding constitutes a major result of the present work.

As we demonstrate below, in a way similar to the Friedel oscillations mechanism proposed by Kohn and Luttinger for simple metals [2], the interplay of attractive and repulsive oscillations of the screened potential can provide the leading mechanism for superconductivity in monolayer NbSe₂.

Gap symmetries and temperature dependence

We next discuss the properties of the superconducting instability mediated by the screened potential. In general, condensates may be formed with finite center-of-mass momentum for Cooper pairs. However, the matrix elements of the screened interaction contributing to pairing are in general complex, with a strongly fluctuating phase resulting from the product of Bloch overlaps, cf. Eq. (10). This tends to favor pairing between time-reversed states, whose Bloch spinors obey the relation $u_{\bar{\sigma},\bar{k}}=u_{\sigma,k}^*$, with -k=: $\bar{k}, -\sigma =: \bar{\sigma}$, resulting in a summation of real and positive contributions to the pairing. We hence retain only the scattering between time reversal partners $(\mathbf{k}, \sigma; \bar{\mathbf{k}}, \bar{\sigma})$, and consider in the following the interaction matrix elements $V_{\mathbf{k},\mathbf{k}',\sigma} := \langle \mathbf{k}',\sigma; \bar{\mathbf{k}}',\sigma' | \hat{V} | \mathbf{k},\sigma; \bar{\mathbf{k}},\bar{\sigma} \rangle$ involving Kramers pairs of Bloch states. This restriction to time-reversal pairs yields a low energy Hamiltonian of the typical BCS form [1]. Performing a mean field approximation, in turn, leads to the familiar BCS gap equation

$$\Delta_{\mathbf{k},\sigma} = -\sum_{\mathbf{k}'} V_{\mathbf{k},\mathbf{k}',\sigma} \Pi(E_{\mathbf{k},\sigma}) \Delta_{\mathbf{k}',\sigma}, \qquad (6)$$

where the pairing function $\Pi(E) = \tanh(\beta E/2)/2E$ depends on the gap through the quasiparticle energies $E_{\mathbf{k},\sigma} = \sqrt{\xi_{\mathbf{k},\sigma}^2 + |\Delta_{\mathbf{k},\sigma}|^2}$, and on the inverse temperature $\beta = 1/k_BT$. To access observables near the phase transition, we linearize Eq. (6) by replacing the excitation energies $E_{\mathbf{k},\sigma}$ in the pairing function by the single-particle energies $\xi_{\mathbf{k},\sigma}$ and solving the resulting linear problem in a range of $\pm \Lambda$ around the Fermi energy [23, 33], cf. Methods. The leading instabilities with the highest T_c are shown in Fig. 3 for the parameter set by He et al. [38] and a truncation to third nearest neighbors of the 1BZ in the calculation of the matrix $V_{\mathbf{G},\mathbf{G'}}^{2D,\mathrm{RPA}}$. They belong to irreducible representations of the symmetry group of the material, which for NbSe₂ is $D_{3\mathrm{h}}$. We find as the dominant pairings two nematic p-like solutions of the E'

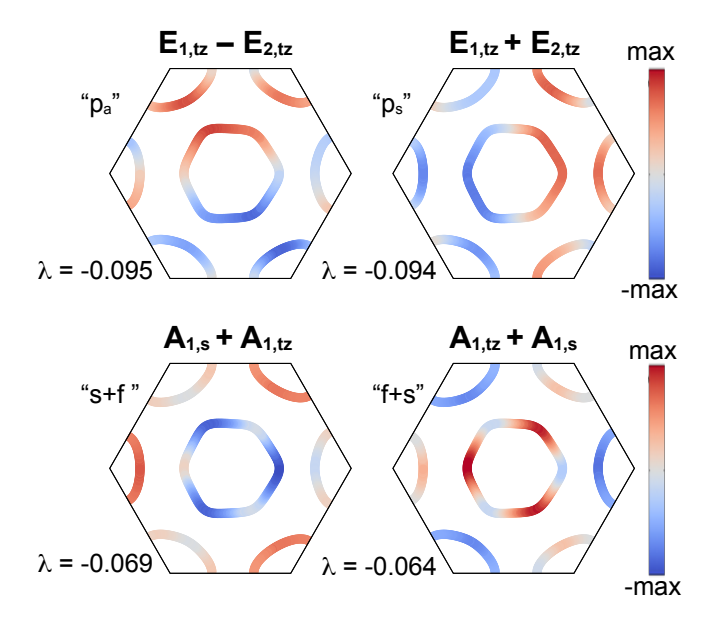


Figure 3. Leading instabilities as found from solving the linearized gap equations. The two solutions with highest critical temperature are nematic. They are mainly provided by the antisymmetric (" p_a ") and symmetric (" p_s ") combination of the basis functions from the E' irrep of the $D_{3\rm h}$ group for the triplet pairing with opposite spins. Although here $p_a \sim p_y$ and $p_s \sim p_x$, if the ratio E'_1/E'_2 of the component changes, the position of the nodes can shift along the Fermi surfaces both for p_a and for p_s . The two following solutions are combinations of the A'_1 z-triplet and A'_1 singlet with the predominantly singlet pairing having a higher critical temperature.

z-triplet type (the singlet admixture is small), in line with the results obtained by Roy et al. [33] for their model interaction. These solutions are followed by the SOC-introduced combinations of the A_1' s-like singlet and f-like z-triplet that were previously discussed as candidates for the superconducting phase of monolayer NbSe₂ [18, 23, 32, 33, 42]. The critical temperatures of these solutions depend on the associated eigenvalues λ of the pairing matrix and the cutoff in energy.

Note that the eigenvalues fall short of the values reported in the literature so far for model Hamiltonians [18, 23, 32, 33, 42]. This is in line with these works using the interaction strength (and the cutoff Λ) as a fit parameter to match the critical temperature observed in experiments, e.g. $T_{\rm c} \approx 2\,{\rm K}$ in epitaxially grown samples [18], and in mechanically exfoliated ones [16]. Solving the linearized gap equation for a cutoff $\Lambda = 100 \,\mathrm{meV}$, we find that the pairing strength required to yield a fixed $T_{\rm c} = 2 \, {\rm K}$ is $\lambda \approx -0.154$. This difference is well within the uncertainty of our calculation due to the differences in the reported band structures for monolayer NbSe₂ [33, 38, 39] and to the impact from the substrate which was not included in our calculation (see also the discussion in the Methods and Section III C in the Supplementary Material). In order to account for these uncertainties

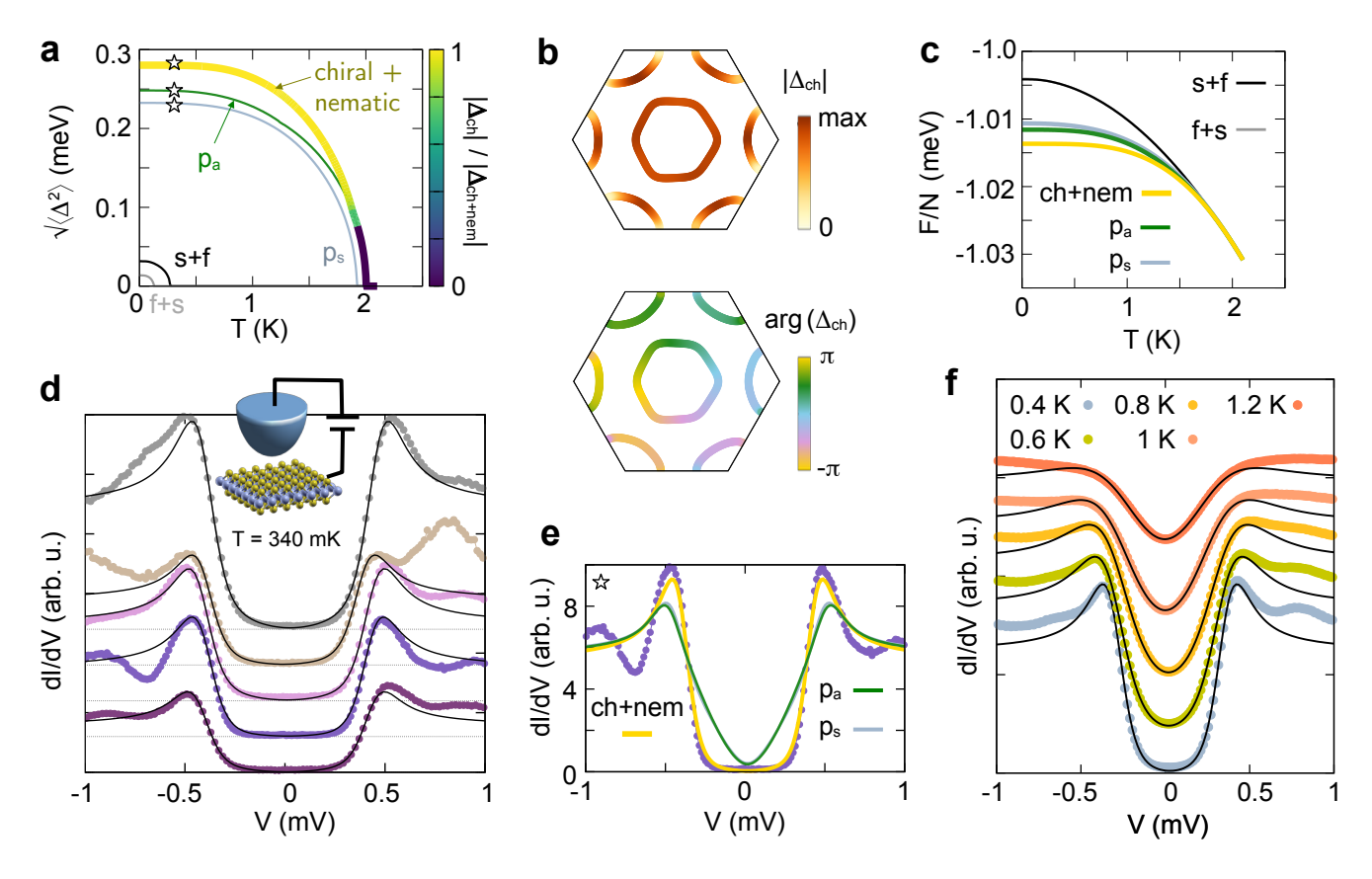


Figure 4. Chiral ground state and comparison with spectroscopic measurements. a Square root of the average square amplitude of the first five gaps solving the self-consistent gap equation as a function of temperature. The thick chiral+nematic curve is the solution with the lowest free energy; its color encodes the fraction of the chiral $(p_a + ip_s)$ contribution in the leading solution. The chiral contribution dominates at low T, while for $T \simeq T_c(p_s)$ only the p_a solution remains and the gap is fully nematic. b At T=340 mK the gap equation predicts a fully gapped chiral phase of p+ip type. The phase of the order parameter winds anticlockwise around each contiguous Fermi surface. c Free energy per electronic state for the first five gap solutions, calculated in the range of energies ± 2 meV. The absence of nodes makes the chiral one the preferred solution at low T. The curves for f+s and s+f gaps are overlapping. d Differential conductance spectra (curves offset for clarity) recorded by STM at 340 mK, at different positions along a NbSe₂ monolayer grown on a bilayer graphene/SiC(0001) substrate. A clear hard gap is observed, which can be fitted using the chiral gap in a. e One of the experimental dI/dV curves in d, fitted with the gaps $\Delta_{k\sigma}$ obtained from the nematic and chiral solutions of the self-consistent gap equation (see the marker in a). A good agreement is found for the chiral solution on the Γ Fermi surface; the nematic ones display a clear V-shape gap that departs from the experimental data. f Experimental traces for different temperatures and corresponding theoretical fits with the leading Δ_{ch+nem} in b, c.

we keep $\Lambda=100$ meV and choose to rescale instead the resulting interaction $\hat{V} \to \gamma \hat{V}$, with $\gamma=1.7$. Furthermore, accounting for an additional phonon-mediated interaction [1, 30], e.g., by considering a momentumindependent interaction $|V_{\rm ph}| \lesssim V^{\rm RPA}(\boldsymbol{q}_{\Gamma})$ would be sufficient to explain this discrepancy, even with unscaled \hat{V} .

The first two eigenvalues are very close and can be considered quasi-degenerate when accounting for a finite quasiparticle lifetime. This allows for the emergence of a chiral gap at temperatures below $T_{\rm c}$ [5]. To which extent a nodal nematic solution or the gapped chiral phase is the preferred ground state, cannot be determined at the level of the linearized gap equation used so far. Instead, we solve the self-consistency equation, Eq. (6), as a function of temperature. Retaining the full

momentum dependence in the gap equation renders the problem highly multi-dimensional. However, the relevant physics is captured by expanding both the interaction and the order parameter in basis functions of the appropriate irreducible representations of the crystal symmetry group [23, 42, 43], and solving a set of coupled equations for the expansion coefficients as a function of the temperature (see Methods). We tracked the evolution of the coefficients down to zero temperature (see Section III A of the Supplementary Material). The square root of the average square gaps (see Methods for the definition) is shown in Fig. 4a. Upon the onset of the second nematic solution p_s , a smooth transition occurs away from the nematic p_a phase, to a fully gapped chiral phase at zero temperature. The magnitude and phase

of this chiral+nematic gap at $T=340\,\mathrm{mK}$, where it is still fully chiral, are displayed in Fig. 4b. The free energy shown in Fig. 4c for the different candidate phases confirms that the chiral+nematic gap is physically stable within the considered temperature range, cf. also the Methods. Hence, similarly to what was possibly observed in TaS₂ [11], we predict a chiral ground state also for monolayer NbSe₂.

A natural question is thus if this finding is compatible with available spectroscopic data. To this end, we turn to our own low-temperature scanning tunneling spectroscopy (STS) measurements carried out on monolayer NbSe₂ on a bilayer graphene/SiC(0001) substrate, see [18] for details of the setup. The measured observable is the tunneling differential conductance (dI/dV), which is proportional to the spectral function of the sample (see Methods and Eq. (29)). The experimental dI/dV spectra recorded at different locations at 340 mK are shown in Fig. 4d and fitted to the tunneling DOS obtained from the chiral gap. As shown in Fig. 1, in NbSe₂ the quasiparticle states near the K and K' valleys arise from the planar $d_{2,\pm 2}$ orbitals, while the ones at the Γ valley have $d_{2,0}$ character and extend farther beyond the NbSe₂ plane. This fact, combined with the sensitivity of STM to states with small in-plane momentum [17, 44], suggests a larger coupling to the states on the Γ Fermi surface compared to those near the K and K' valleys. The theoretical differential conductance shown in Fig. 4d is calculated using the coupling to the Γ and K Fermi pockets as free parameters (see Methods).

In Fig. 4e we show the fit to a representative experimental $\mathrm{d}I/\mathrm{d}V$ spectrum recorded at 340 mK, using both the chiral and the nematic solutions on the Γ Fermi pocket. The presence of nodal lines in the nematic phases is reflected in a V-like shape of the gap, which was not observed in the experiment. Such a shape was instead recently reported for spectroscopy experiments on monolayer 1H-TaS₂ [45]. Also for the remaining gap symmetries (s+f and f+s) no agreement with the experiment is found (see Section III B of the Supplementary Material).

Finally, the temperature evolution of the differential conductance at one fixed tip location is shown in Fig. 4f. The agreement with the theoretical curves which use the temperature dependence of the gap as displayed in Fig. 4a is remarkable.

While one can confidently state that the STS data are consistent with the theory presented in this work, and in particular with a chiral p-like gap at the lowest temperatures, it is clear that they alone are not conclusive evidence for this pairing symmetry. In fact, a conventional s-like BCS gap would yield a reasonable agreement with the data as well [18]. Additional insight is provided by nematic features observed in resistance experiments [24, 46], with critical temperature dependent on the direction of the in-plane magnetic fields, in agreement with our prediction of a nematic phase near $T_{\rm c}$. These observations suggest that the chiral phase should be the most probable gapped phase observed in the STS

experiment. To gather further evidence, we propose testing other signatures of a chiral phase, which can be revealed in quasiparticle interference patterns [47] or in the enhancement of the zero bias conductance near the edges of superconducting domains [9].

METHODS

Low energy model

We consider the low-energy Hamiltonian for the metallic valence band of monolayer ${\rm NbSe_2}$

$$\hat{H}_{VB} = \sum_{\mathbf{k},\sigma} \xi_{\mathbf{k},\sigma} \hat{c}_{\mathbf{k},\sigma}^{\dagger} \hat{c}_{\mathbf{k},\sigma} + \hat{V}, \qquad (7)$$

where the first term describes independent Bloch electrons in the valence band with energies $\xi_{\boldsymbol{k},\sigma}$, and $\hat{c}_{\boldsymbol{k},\sigma}^{(\dagger)}$ are the creation and annihilation operators of Bloch electrons with crystal momentum \boldsymbol{k} . The second term is the screened Coulomb interaction which, in the position representation $(1 \equiv \boldsymbol{r}, \sigma)$, is defined by a Dyson equation for its matrix elements $V(1,2) = \langle (1,2)|\hat{V}|(1,2)\rangle$ as

$$V(1,2) = V_0(1,2) + \int d(3,4)V_0(1,3)P(3,4)V(4,2),$$
(8)

with $V_0(1,2)$ the matrix elements of the unscreened interaction and P the polarizability of the interacting system. We consider a trigonal 2D lattice with periodic boundary conditions composed of N prismatic unit cells of area Ω and height L with sample volume $\mathcal{V}=N\Omega L$. The derivation of Eq. (2) from Eq. (8) can be found in the Supplementary Material.

Screened interaction in RPA

We treat the screening at the RPA level, where the full polarizability in Eq. (8) is replaced with the noninteracting polarizability tensor given by Eq. (4) where

$$\chi_{\sigma}(\mathbf{p} + \mathbf{q}, \mathbf{p}; \omega) = \frac{1}{N\Omega} \frac{f(\xi_{\mathbf{p}+\mathbf{q},\sigma}) - f(\xi_{\mathbf{p},\sigma})}{\omega + \xi_{\mathbf{p}+\mathbf{q},\sigma} - \xi_{\mathbf{p},\sigma} + i\eta}, \quad (9)$$

f is the Fermi function evaluated from the chemical potential μ and the overlaps \mathcal{F} are defined in Eq. (5). For momenta \mathbf{k}/\mathbf{k}' outside of the first Brillouin zone, Eq. (5) is modified by decomposing $\mathbf{k} = \mathcal{P}(\mathbf{k}) + \mathcal{Q}(\mathbf{k})$ (see Fig. S.3 in the Supplementary Material), where \mathcal{P} projects onto the reciprocal lattice, \mathcal{Q} projects onto the associated crystal momentum and using $\mathbf{u}_{\mathbf{k},\sigma}(\mathbf{r}) = e^{i\mathcal{P}(\mathbf{k})\cdot \mathbf{r}}\mathbf{u}_{\mathcal{Q}(\mathbf{k}),\sigma}(\mathbf{r})$. We express the interaction \hat{V} entering Eq. (7) in the Bloch basis. It holds for the statically screened Coulomb interaction between Bloch states (see

the Supplementary Material for the full derivation),

$$\langle \mathcal{Q}(\boldsymbol{k}+\boldsymbol{q}), \sigma; \mathcal{Q}(\boldsymbol{k}'-\boldsymbol{q}), \sigma' | \hat{V} | \boldsymbol{k}, \sigma; \boldsymbol{k}', \sigma' \rangle =$$

$$\frac{1}{N\Omega} \sum_{\boldsymbol{G}, \boldsymbol{G}'} V_{\boldsymbol{G}, \boldsymbol{G}'}^{\text{2D,RPA}}(\boldsymbol{q}; 0^{+}) \mathcal{F}_{\boldsymbol{k}+\boldsymbol{q}, \boldsymbol{k}}^{\sigma}(-\boldsymbol{G}) \mathcal{F}_{\boldsymbol{k}'-\boldsymbol{q}, \boldsymbol{k}'}^{\sigma'}(\boldsymbol{G}'),$$
(10)

where k, k' and q are in-plane momenta restricted to the first Brillouin zone. Noting that the dominant contribution to the matrix element is due to the first few nearest neighbor sites (see Section II D of the Supplementary Material for a discussion) we introduce an effective interaction potential

$$\langle \mathcal{Q}(\boldsymbol{k}+\boldsymbol{q}), \sigma; \mathcal{Q}(\boldsymbol{k}'-\boldsymbol{q}), \sigma' | \hat{V} | \boldsymbol{k}, \sigma; \boldsymbol{k}', \sigma' \rangle =$$
(11)

$$\approx \frac{1}{N\Omega} \left(\sum_{\boldsymbol{G}, \boldsymbol{G}'} V_{\boldsymbol{G}, \boldsymbol{G}'}^{\text{2D,RPA}}(\boldsymbol{q}) \right) \mathcal{F}_{\boldsymbol{k}+\boldsymbol{q}, \boldsymbol{k}}^{\sigma}(\boldsymbol{0}) \mathcal{F}_{\boldsymbol{k}'-\boldsymbol{q}, \boldsymbol{k}'}^{\sigma'}(\boldsymbol{0}')$$

$$=: \frac{1}{N\Omega} V^{\text{RPA}}(\boldsymbol{q}) \mathcal{F}_{\boldsymbol{k}+\boldsymbol{q}, \boldsymbol{k}}^{\sigma}(\boldsymbol{0}) \mathcal{F}_{\boldsymbol{k}'-\boldsymbol{q}, \boldsymbol{k}'}^{\sigma'}(\boldsymbol{0}'),$$

where we restrict G, G' to the range where $\mathcal{F}(G) \approx \mathcal{F}(0)$ holds, i.e., up to third nearest neighboring Brillouin zones. This effective interaction potential enables a discussion of the screened interaction on the lattice in terms of a simple q-dependent quantity, but is *not* used for the calculation of the pairing, where we keep the dependence of the Bloch factors \mathcal{F} on G.

Linearized gap equation

To access the possible superconducting instabilities described by Eq. (6), we solve a linearized form of the gap equation. First, we project the gap equations on the Fermi surfaces by introducing a local density of states $\rho_{\mathbf{k},\sigma}$ along the Fermi surfaces. We restrict the allowed momenta \mathbf{k}' in Eq. (6) to a range around the Fermi surfaces given by a cutoff $\pm \Lambda$ in energy. Next, we convert the sum over the transverse component $\mathbf{k}' - \mathbf{k}_{\mathrm{F}}$ into an integral in energy over this range $[-\Lambda, \Lambda]$. Assuming that the gap and the interaction vary slowly in this thin shell around each Fermi surface, we can approximate $\Delta_{\mathbf{k}',\sigma} \approx \Delta_{\mathbf{k}_{\mathrm{F}},\sigma}$ and $V_{\mathbf{k},\mathbf{k}',\sigma} \approx V_{\mathbf{k},\mathbf{k}_{\mathrm{F}},\sigma}$. The resulting gap equation with \mathbf{k},\mathbf{k}' on the Fermi surfaces takes the form

$$\Delta_{\mathbf{k},\sigma} = -\sum_{\mathbf{k}' \in FS} V_{\mathbf{k},\mathbf{k}',\sigma} \int_{-\Lambda}^{\Lambda} d\xi \rho_{\mathbf{k}',\sigma}(\xi) \Pi(E_{\mathbf{k}'\sigma}) \Delta_{\mathbf{k}',\sigma},$$
(12)

with the pairing function $\Pi(E)=\tanh(\beta E/2)/2E$. Close to $T_{\rm c}$ we have $\Pi(E)\approx\Pi(\xi)$ and Eq. (12) becomes a set of linear equations. There, the problem of finding the shape of the order parameter along the Fermi surfaces is equivalent to determining the kernel of a matrix \mathbb{M}_{σ} , whose indices are the momenta $k_{\rm F}$ on the Fermi surface, as

$$\mathbb{M}_{\sigma}\vec{\Delta}_{\sigma} = 0, \tag{13}$$

where, $\forall k, k' \in FS$,

$$(\mathbb{M}_{\sigma})_{\mathbf{k},\mathbf{k}'} = \delta_{\mathbf{k},\mathbf{k}'} + V_{\mathbf{k},\mathbf{k}',\sigma}\rho_{\mathbf{k}',\sigma}\alpha^{0}(T,\Lambda), \qquad (14)$$

$$\alpha^{0}(T,\Lambda) = \int_{0}^{\Lambda} d\xi \frac{\tanh(\beta \xi/2)}{\xi} \,. \tag{15}$$

Here, we assumed a flat density of states $\rho_{\mathbf{k},\uparrow}(\xi) \approx \rho_{\mathbf{k},\uparrow}$ within the energy range $\pm \Lambda$ around the chemical potential. We rewrite \mathbb{M}_{σ} by factoring out the energy integral α^0 in the second summand as

$$\mathbb{M}_{\sigma} = \mathbb{1} + \alpha^{0}(T, \Lambda)\mathbb{U}_{\sigma}, \qquad (16)$$

where \mathbb{U}_{σ} is the pairing matrix containing the interaction and local density of states along the Fermi surfaces. The possible superconducting pairings solving Eq. (13) are the eigenvectors of \mathbb{U}_{\uparrow} with the corresponding eigenvalues λ_i fulfilling

$$\lambda_i = -1/\alpha^0(T_{c,i}, \Lambda), \qquad (17)$$

and $T_{c,i}$ the critical temperature of the respective instability. The cutoff Λ sets an energy scale against which to measure the gaps and T_c , similar to the Debye frequency in the usual BCS-theory [1]. In general, not all eigenvectors of \mathbb{U}_{σ} found in this way correspond to physically stable situations [48]. Similarly, the requirement of vanishing $\Delta_{k,\sigma}$ close to $T_{c,i}$ is only fulfilled if no other superconducting phase with higher T_c is present. As such, we expect only the solution with the highest T_c to be realized. Due to the monotonic nature of $\alpha^0(T,\Lambda)$ as a function of both T and Λ , the solution with the highest critical temperature always corresponds to the lowest negative eigenvalue λ of the pairing matrix. As Λ is a model parameter, we classify and discuss the strength of the different instabilities by their eigenvalues λ_i .

Expansion of the temperature-dependent gap equation in basis functions

To investigate how the gaps evolve at temperatures below T_c , we solve Eq. (12) without linearizing. Since we want to use the approximations $\Delta_{\mathbf{k}',\sigma} \approx \Delta_{\mathbf{k}_{\mathrm{F}},\sigma}$ and $V_{\mathbf{k},\mathbf{k}',\sigma} \approx V_{\mathbf{k},\mathbf{k}_{\mathrm{F}},\sigma}$, we fix the cutoff to the value of $\Lambda = 0.1\,\mathrm{eV}$ which, together with the rescaling of the screened interaction to $\hat{V}_{\gamma} := \gamma \hat{V} = 1.7 \hat{V}$ as discussed in the main text, yields $T_{\rm c}=2$ K. This enables us to fit to the experimental T_c while retaining the shape of the interaction as found from our calculation of the screened Coulomb interaction. Since the macroscopic polarizability $P_{0,0}$ calculated from DFT (cf. Section I B of the Supplementary Material) is even lower at intermediate momentum transfers than our results from a tight-binding calculation, it is plausible that the screened interaction is indeed stronger than our \hat{V} . We expand the gap for one spin species in terms of a restricted set of basis functions, corresponding to the irreducible representations of the symmetry group D_{3h} , as

$$\forall_{\mathbf{k}\in\pi}: \quad \Delta_{\mathbf{k},\uparrow} = \sum_{\mu} f_{\mu}^{\pi}(\mathbf{k}) \Delta_{\mu}^{\pi}, \qquad (18)$$

where μ labels basis functions and $\pi \in \{\Gamma, K\}$ the Fermi surfaces [23, 36]. We orthonormalize our basis functions with respect to the number N_{π} of momenta on each Fermi surface π to satisfy

$$\langle f_{\mu}^{\pi}, f_{\mu'}^{\pi} \rangle_{\pi} := \frac{1}{N_{\pi}} \sum_{\mathbf{k} \in \pi} f_{\mu'}^{\pi}(\mathbf{k}) f_{\mu}^{\pi}(\mathbf{k}) = \delta_{\mu, \mu'}.$$
 (19)

Using this orthogonality, we reduce the dimensionality of the self-consistency problem drastically by projecting the gap equation into a form that couples only the expansion coefficients Δ^{π}_{μ} [23]. It reads

$$\Delta_{\mu}^{\pi} = -\frac{1}{N_{\pi}} \sum_{\pi',\mu'} \sum_{\substack{\mathbf{k} \in \pi \\ \mathbf{k}' \in \pi'}} f_{\mu}^{\pi}(\mathbf{k}) V_{\mathbf{k},\mathbf{k}',\uparrow} \rho_{\mathbf{k}',\uparrow} \alpha_{\mathbf{k}'}^{\pi'} f_{\mu'}^{\pi'}(\mathbf{k}') \Delta_{\mu'}^{\pi'},$$
(20)

where the pairing strength $\alpha_{\mathbf{k}}^{\pi}$ is given by

$$\alpha_{\mathbf{k}}^{\pi} = \int_{0}^{\Lambda} d\xi \, \frac{\tanh(\beta E(\xi, \Delta_{\mathbf{k}}^{\pi})/2)}{E(\xi, \Delta_{\mathbf{k}}^{\pi})} \,. \tag{21}$$

At T_c , the pairing strength $\alpha_{\mathbf{k}}^{\pi}$ becomes independent of \mathbf{k} and π . In this case, the orthogonality Eq. (19) yields a linearized gap equation for the expansion coefficients

$$\Delta_{\mu}^{\pi} = -\alpha^{0} \sum_{\pi', \mu'} U_{\mu, \mu'}^{\pi, \pi'} \Delta_{\mu}^{\pi'}, \qquad (22)$$

where the pairing matrix $\mathbb U$ in this representation is given by

$$U_{\mu,\mu'}^{\pi,\pi'} = \frac{1}{N_{\pi}} \sum_{\mathbf{k} \in \pi, \mathbf{k}' \in \pi'} f_{\mu}^{\pi}(\mathbf{k}) V_{\mathbf{k},\mathbf{k}',\uparrow} \rho_{\mathbf{k}',\uparrow} f_{\mu'}^{\pi'}(\mathbf{k}'). \quad (23)$$

To account for the mixing between different symmetries due to the k dependence of α_{k}^{π} below T_{c} , we insert a unity in Eq. (20) to arrive at

$$\Delta^{\pi}_{\mu} = -\sum_{\pi', \mu', \mu''} U^{\pi, \pi'}_{\mu, \mu'} \Upsilon^{\pi'}_{\mu', \mu''} \Delta^{\pi'}_{\mu''}, \qquad (24)$$

where the mixing of different basis functions is described by

$$\Upsilon^{\pi}_{\mu,\mu'} = \frac{1}{N_{\pi}} \sum_{\mathbf{k} \in \pi} f^{\pi}_{\mu}(\mathbf{k}) \alpha^{\pi}_{\mathbf{k}} f^{\pi}_{\mu'}(\mathbf{k}). \tag{25}$$

For an incomplete set of basis functions this insertion of unity becomes approximate, but in our case still suffices to capture the weak mixing between basis functions induced by $\alpha_{\mathbf{k}}^{\pi}$. As such, we employ Eq. (24) to numerically determine the evolution of the solutions obtained from

the linearized equations below their $T_{c,i}$. The basis functions we used and the temperature dependence curves for the respective expansion coefficients are shown in Section III A of the Supplementary Material.

The chiral solution is defined as

$$\Delta_{\rm ch} = \frac{||\Delta_s||}{||\Delta_a||} \Delta_a + i\Delta_s,\tag{26}$$

where $||\Delta|| := \sqrt{\sum_{\pi=G,K} \langle \Delta, \Delta \rangle_{\pi}}$ with the scalar product defined in Eq. (19). The Δ_a component is renormalized so that both nematic solutions enter with the same weight. The admixture of $\Delta_{\rm ch}$ in the leading solution $\Delta_{\rm ch+nem}$ in Fig. 4c is defined as

$$\frac{\Delta_{\rm ch}}{\Delta_{\rm ch+nem}} := \frac{\left|\sum_{\pi=\Gamma,K} \langle \Delta_{\rm ch}, \Delta_{\rm ch+nem} \rangle_{\pi}\right|}{\left|\left|\Delta_{\rm ch+nem}\right|\right| \left|\left|\Delta_{\rm ch}\right|\right|}.$$
 (27)

The square root of mean squared Δ shown in Fig. 4a for each gap symmetry is $\sqrt{\langle \Delta^2 \rangle} \equiv ||\Delta||$.

A. Free energy for self-consistent solutions

The free energy of a superconductor with gap $\Delta_{{m k}\sigma}$ can be written as

$$F = \frac{1}{2} \sum_{k\sigma} \left(\xi_{k\sigma} - E_{k\sigma} + \Pi(E_{k\sigma}) |\Delta_{k\sigma}|^2 \right) - k_B T \sum_{k\sigma} \ln \left(1 + e^{-E_{k\sigma}/k_B T} \right).$$
 (28)

Note that this free energy is written assuming that the gap obeys the self-consistent equations (see Section III of the Supplementary Material comments on its derivation). It cannot be used to find the physical gaps by minimization with respect to $\Delta_{k\sigma}$, but does yield the correct result once a solution is found by solving the self-consistent gap equations [48]. We therefore use it to rank the solutions by their free energy gain within the energy window of ± 2 meV where the contributions of different gap symmetries are distinguishable.

Experimental setup and methods

NbSe₂ monolayers₂ were grown on graphitized (bilayer graphene) on 6H-SiC(0001) by molecular beam epitaxy (MBE) at a base pressure of $\sim 2 \cdot 10^{-10}$ mbar in our home-made ultrahigh-vacuum (UHV) MBE system. SiC wafers with resistivities $\rho \sim 120\,\Omega{\rm cm}$ were used [49]. Reflective high-energy electron diffraction (RHEED) was used to monitor the growth of the NbSe layer₂. During the growth, the bilayer graphene/SiC substrate was kept at 580° C. High-purity Nb (99.99%) and Se (99.999%) were evaporated using an electron beam evaporator and a standard Knudsen cell, respectively. The Nb:Se flux ratio was kept at 1:30, while evaporating Se led to a pressure of

 $\sim 5 \cdot 10^{-9}\,\mathrm{mbar}$ (Se atmosphere). Samples were prepared using an evaporation time of 30 min to obtain a coverage of ~ 1 ML. To minimize the presence of atomic defects, the evaporation of Se was subsequently kept for an additional 5 minutes. Atomic force microscopy (AFM) under ambient conditions was routinely used to optimize the morphology of the NbSe₂ layers. The samples used for AFM characterization were not further used for the scanning tunneling microscope (STM). Lastly, to transfer the samples from our UHV-MBE chamber to our STM, they were capped with a $\sim 10\,\mathrm{nm}$ amorphous film of Se, which was subsequently removed by annealing at the STM under UHV conditions at 280 ° C.

Scanning tunneling microscopy/spectroscopy experiments were carried out in a commercial low-temperature, high magnetic field (11 T) UHV-STM from Unisoku (model USM1300) operated at $T = 0.34 \,\mathrm{K}$ unless otherwise stated. STS measurements (using Pt/Ir tips) were performed using the lock-in technique with typical ac modulations of $20 - 40 \,\mu\text{V}$ at $833 \,\text{Hz}$. All data were analyzed and rendered using WSxM software [50]. To avoid tip artifacts in our STS measurements, the STM tips used for our experiments were previously calibrated on a Cu(111) surface. A tip was considered calibrated only when tunneling spectroscopy performed on Cu(111) showed a sharp surface state onset at $-0.44\,\mathrm{eV}$ followed by a clean and monotonic decay of the differential conductance signal (i.e. dI/dV). In addition to this, we also inspected the differential conductance within $\pm 10\,\mathrm{mV}$ to avoid strong variations around the Fermi energy.

Comparison to experimental tunneling spectroscopy

For spectroscopy in the tunneling regime with a normal metal tip, the differential conductance is given by

$$G(V) = \sum_{\mathbf{k},\sigma} C_{\mathbf{k}\sigma} \int_{-\infty}^{\infty} \frac{\mathrm{d}E}{2\pi} A_{\mathbf{s}}(\mathbf{k},\sigma; E) \left(-\frac{\partial f(E + eV)}{\partial E} \right) ,$$
(29)

where A_s is the spectral function of the superconductor. The coupling $C_{\boldsymbol{k}\sigma}$ accounts for the spectral function of the tip and the tunneling overlap between the tip's evanescent states and quasiparticle states from the superconductor with momentum \boldsymbol{k} and spin σ . We do not expect the coupling to vary much on any given Fermi surface π , and as such we approximate $C_{\boldsymbol{k},\sigma}\approx C_{\pi}$. However, due to the different orbital composition of the quasiparticle states at the K, K' valleys and at the Γ surface, cf. Fig. 1b, the coupling constant will be in general different. In particular, since the $d_{2,0}$ orbital extends farthest out of plane and the STM favors states with small in-plane momentum, we expect $C_{\Gamma}\gg C_{K}$.

In the tunneling regime, where the experimental data was taken, the lifetime of the quasiparticles is weakly affected by the coupling to the tip and the spectral function can be approximated with the local density of states of the quasiparticles, $A_s(\mathbf{k}, \sigma, E) = 2\pi D_{\mathbf{k}, \sigma}(E)$. The tunneling to each of the Fermi surfaces represents a distinct transport channel, whose strength is given by the sum over the local density of states

$$D_{\pi,\sigma}(E) = \sum_{\mathbf{k} \in \pi} D_{\mathbf{k},\sigma}(E). \tag{30}$$

The latter are modeled by assuming a BCS form factor modifying the local density of states $\rho_{k,\sigma}$ in the normal conducting state as

$$D_{\mathbf{k},\sigma}(E) = \rho_{\mathbf{k},\sigma} \operatorname{Re} \sqrt{\frac{E^2}{E^2 - |\Delta_{\mathbf{k},\sigma}|^2}}.$$
 (31)

In the absence of magnetic fields, we can assume that due to time reversal symmetry $D_{\pi,\sigma} = D_{\pi}/2$ and $C_{\pi,\sigma} = C_{\pi}$. As such, Eq. (29) predicts for the total differential conductance a superposition of contributions from the distinct transport channels with weights provided by the couplings C_{π} as

$$G(V) \approx \sum_{\pi} C_{\pi} G_{\pi}(V) ,$$
 (32)

$$G_{\pi}(V) = \int_{-\infty}^{\infty} dE \ D_{\pi}(E) \left(-\frac{\partial f(E + eV)}{\partial E} \right).$$
 (33)

For low temperature, the form of the gap on each separate Fermi surface results in characteristic signatures in the differential conductance of the respective transport channel. We use as a fit function this superposition of the differential conductance of the individual transport channels. For the gaps on the Fermi surfaces $\Delta_{k,\sigma}$, we use the form of the gaps as found from Eq. (24) at the experimental temperature T_{exp} (T=0 for the A'_1 gaps) and allow for a fit of the amplitude by a common rescaling of all $\Delta_{\mathbf{k},\sigma}$ by a parameter A as $\Delta_{\mathbf{k},\sigma} \to A\Delta_{\mathbf{k},\sigma}$. The latter is introduced to take care of the uncertainty of the actual experimentally realized $T_{\rm c}$ and the rescaling factor γ of the interaction. To qualitatively account for additional sources of broadening in the experiment, we use an effective temperature $T_{\rm eff} = 1.25 T_{\rm exp}$ for the calculation of the derivative in Eq. (33). For the fitting we use the trust region reflective algorithm as implemented in SciPy's "curve_fit" routine. We consider a range of $\pm 0.7\,\mathrm{mV}$ containing the main coherence peaks, but not the satellite features due to Leggett modes [18], which are not accounted for in our theory. The resulting fit parameters are listed in Table I in Section III B of the Supplementary Material. The best fits for the solutions associated with the E^\prime irreducible representation are obtained by considering strongly selective coupling of the tip to the Γ pockets. This contrasts with the solutions associated to the A'_1 irreducible representation. There the fit to the experiment could only be obtained with strongly selective coupling to the K pockets, which cannot be justified on physical grounds.

Data availability

All data shown in the figures and underpinning the shown results will be made available upon reasonable request to the authors. The code used to generate the shown data is available upon request.

Acknowledgments

The work of Julian Siegl and Anton Bleibaum was funded by project B09 within CRC 1277 and RTG 2905 - 502572516 of the Deutsche-Forschungsgemeinschaft, respectively. M.K. appreciates discussions with Timon Moško and acknowledges support from the Interdisciplinary Centre for Mathematical and Computational Modelling (ICM), University of Warsaw (UW), within grant no. G83-27 and the financial support from the National Center for Research and Development (NCBR) under the V4-Japan project BGapEng V4-JAPAN/2/46/BGapEng/2022. M.M.U. acknowledges support by the ERC Starting grant LINKSPM (Grant #758558) and by the grant PID2023-153277NB-I00

funded by the Spanish Ministry of Science, Innovation and Universities. M.M. appreciates helpful discussions with Fernando de Juan, Martin Gmitra and Cosimo Gorini, and acknowledges thankfully the help of Andrea Donarini and Marko Milivojevic in constructing the basis functions.

Author contributions

J.Si. and M.M. performed the analytical and numerical tight-binding calculations. M.K. calculated the DFT band structure and polarizability. W.W. and M.M.U. performed the STM/STS experiments on the monolayer NbSe₂. A.B. performed the fitting to the experimental data. M.G. conceived the project, leading with M.M. the theoretical analysis with support from J.Si. and J.Sc.; M.M.U. was responsible for the experimental part of this work. The manuscript was written by M.G., J.Si. and M.M. with contributions from all other authors.

- Bardeen, J., Cooper, L. N., Schrieffer, J. R. "Theory of Superconductivity." *Phys. Rev.*, 108 (5), 1175–1204 (1957). doi:10.1103/PhysRev.108.1175.
- [2] Kohn, W., Luttinger, J. M. "New Mechanism for Superconductivity." *Phys. Rev. Lett.*, 15 (12), 524–526 (1965). doi:10.1103/PhysRevLett.15.524.
- [3] Friedel, J. "XIV. The Distribution of Electrons Round Impurities in Monovalent Metals." London Edinburgh Philos. Mag. & J. Sci., 43 (337), 153–189 (1952). doi: 10.1080/14786440208561086.
- [4] Scalapino, D. J. "A Common Thread: The Pairing Interaction for Unconventional Superconductors." Rev. Mod. Phys., 84 (4), 1383–1417 (2012). doi: 10.1103/RevModPhys.84.1383.
- [5] Kallin, C., Berlinsky, J. "Chiral Superconductors." Rep. Prog. Phys., 79 (5), 054502 (2016). doi:10.1088/0034-4885/79/5/054502.
- [6] Mackenzie, A. P., Scaffidi, T., Hicks, C. W., Maeno, Y. "Even Odder after Twenty-Three Years: The Superconducting Order Parameter Puzzle of Sr2RuO4." Npj Quantum Mater., 2 (1), 1–9 (2017). doi:10.1038/s41535-017-0045-4.
- Black-Schaffer, A. M., Honerkamp, C. "Chiral D-Wave Superconductivity in Doped Graphene." J. Phys.: Condens. Matter, 26 (42), 423201 (2014). doi:10.1088/0953-8984/26/42/423201.
- [8] Nandkishore, R., Levitov, L. S., Chubukov, A. V. "Chiral Superconductivity from Repulsive Interactions in Doped Graphene." *Nature Phys*, 8 (2), 158–163 (2012). doi: 10.1038/nphys2208.
- [9] Ming, F., Wu, X., Chen, C., Wang, K. D., Mai, P., Maier, T. A., Strockoz, J., Venderbos, J. W. F., González, C., Ortega, J., Johnston, S., Weitering, H. H. "Evidence for Chiral Superconductivity on a Silicon Surface." Nat. Phys., 19 (4), 500–506 (2023). doi:10.1038/s41567-022-01889-1.
- [10] Ribak, A., Skiff, R. M., Mograbi, M., Rout, P. K., Fischer, M. H., Ruhman, J., Chashka, K., Dagan, Y., Kanigel, A. "Chiral superconductivity in the alternate

- stacking compound 4Hb-TaS₂." *Science*, 6 (13), eaax9480 (2020). doi:10.1126/sciadv.aax9480.
- [11] Silber, I., Mathimalar, S., Mangel, I., Nayak, A., Green, O., Avraham, N., Beidenkopf, H., Feldman, I., Kanigel, A., Klein, A., Goldstein, M., Banerjee, A., Sela, E., Dagan, Y. "Two-Component Nematic Superconductivity in 4Hb-TaS2." Nat. Commun., 15 (2024). doi: 10.1038/s41467-024-45169-3.
- [12] Wan, Z., Qiu, G., Ren, H., Qian, Q., Li, Y., Xu, D., Zhou, J., Zhou, J., Zhou, B., Wang, L., Yang, T.-H., Sofer, Z., Huang, Y., Wang, K. L., Duan, X. "Unconventional superconductivity in chiral molecule—TaS₂ hybrid superlattices." *Nature*, 632 (8023), 69–74 (2024). doi: 10.1038/s41586-024-07625-4.
- [13] Xu, X., Yao, W., Xiao, D., Heinz, T. F. "Spin and Pseudospins in Layered Transition Metal Dichalcogenides." Nat. Phys., 10 (5), 343–350 (2014). doi: 10.1038/nphys2942.
- [14] Xi, X., Wang, Z., Zhao, W., Park, J.-H., Law, K. T., Berger, H., Forró, L., Shan, J., Mak, K. F. "Ising pairing in superconducting NbSe2 atomic layers." *Nat. Phys.*, 12 (2), 139–143 (2016). doi:10.1038/nphys3538.
- [15] Zhang, D., Falson, J. "Ising Pairing in Atomically Thin Superconductors." *Nanotechnology*, 32 (50), 502003 (2021). doi:10.1088/1361-6528/ac238d.
- [16] Cao, Y., Mishchenko, A., Yu, G. L., Khestanova, E., Rooney, A. P., Prestat, E., Kretinin, A. V., Blake, P., Shalom, M. B., Woods, C., Chapman, J., Balakrishnan, G., Grigorieva, I. V., Novoselov, K. S., Piot, B. A., Potemski, M., Watanabe, K., Taniguchi, T., Haigh, S. J., Geim, A. K., Gorbachev, R. V. "Quality Heterostructures from Two-Dimensional Crystals Unstable in Air by Their Assembly in Inert Atmosphere." Nano Lett., 15 (8), 4914–4921 (2015). doi:10.1021/acs.nanolett.5b00648.
- [17] Ugeda, M. M., Bradley, A. J., Zhang, Y., Onishi, S., Chen, Y., Ruan, W., Ojeda-Aristizabal, C., Ryu, H., Edmonds, M. T., Tsai, H.-Z., Riss, A., Mo, S.-K., Lee, D., Zettl, A., Hussain, Z., Shen, Z.-X., Crommie, M. F. "Characterization of Collective Ground States in Single-

- Layer NbSe2." Nat. Phys., 12 (1), 92–97 (2016). doi: 10.1038/nphys3527.
- [18] Wan, W., Dreher, P., Muñoz-Segovia, D., Harsh, R., Guo, H., Martínez-Galera, A. J., Guinea, F., de Juan, F., Ugeda, M. M. "Observation of Superconducting Collective Modes from Competing Pairing Instabilities in Single-Layer NbSe2." Adv. Mat., 34 (41), 2206078 (2022). doi:10.1002/adma.202206078.
- [19] Frigeri, P. A., Agterberg, D. F., Koga, A., Sigrist, M. "Superconductivity without Inversion Symmetry: MnSi versus CePt₃Si." *Phys. Rev. Lett.*, 92 (9), 097001 (2004). doi:10.1103/PhysRevLett.92.097001.
- [20] Xi, X., Berger, H., Forró, L., Shan, J., Mak, K. F. "Gate Tuning of Electronic Phase Transitions in Two-Dimensional NbSe₂." *Phys. Rev. Lett.*, 117 (10), 106801 (2016). doi:10.1103/PhysRevLett.117.106801.
- [21] Ilić, S., Meyer, J. S., Houzet, M. "Enhancement of the Upper Critical Field in Disordered Transition Metal Dichalcogenide Monolayers." *Phys. Rev. Lett.*, 119 (11), 117001 (2017). doi:10.1103/PhysRevLett.119.117001.
- [22] Möckli, D., Khodas, M. "Magnetic-field induced s+if pairing in Ising superconductors." *Phys. Rev. B*, 99 (18), 180505 (2019). doi:10.1103/PhysRevB.99.180505.
- [23] Shaffer, D., Kang, J., Burnell, F. J., Fernandes, R. M. "Crystalline nodal topological superconductivity and Bogolyubov Fermi surfaces in monolayer NbSe₂." *Phys. Rev. B*, 101 (22), 224503 (2020). doi: 10.1103/PhysRevB.101.224503.
- [24] Cho, C.-w., Lyu, J., An, L., Han, T., Lo, K. T., Ng, C. Y., Hu, J., Gao, Y., Li, G., Huang, M., Wang, N., Schmalian, J., Lortz, R. "Nodal and Nematic Superconducting Phases in NbSe₂ Monolayers from Competing Superconducting Channels." *Phys. Rev. Lett.*, 129 (8), 087002 (2022). doi:10.1103/PhysRevLett.129.087002.
- [25] Johannes, M. D., Mazin, I. I., Howells, C. A. "Fermi-surface nesting and the origin of the charge-density wave in NbSe₂." Phys. Rev. B, 73 (20), 205102 (2006). doi: 10.1103/PhysRevB.73.205102.
- [26] Xi, X., Zhao, L., Wang, Z., Berger, H., Forró, L., Shan, J., Mak, K. F. "Strongly enhanced charge-density-wave order in monolayer NbSe2." Nat. Nanotechnol., 10 (9), 765–769 (2015). doi:10.1038/nnano.2015.143.
- [27] Heil, C., Poncé, S., Lambert, H., Schlipf, M., Margine, E. R., Giustino, F. "Origin of Superconductivity and Latent Charge Density Wave in NbS 2." Phys. Rev. Lett., 119 (8), 087003 (2017). doi: 10.1103/PhysRevLett.119.087003.
- [28] Sanna, A., Pellegrini, C., Liebhaber, E., Rossnagel, K., Franke, K. J., Gross, E. K. U. "Real-Space Anisotropy of the Superconducting Gap in the Charge-Density Wave Material 2H-NbSe2." Npj Quantum Mater., 7 (1), 6 (2022). doi:10.1038/s41535-021-00412-8.
- [29] Zheng, F., Feng, J. "Electron-phonon coupling and the coexistence of superconductivity and charge-density wave in monolayer NbSe₂." *Phys. Rev. B*, 99 (16), 161119 (2019). doi:10.1103/PhysRevB.99.161119.
- [30] Das, S., Paudyal, H., Margine, E. R., Agterberg, D. F., Mazin, I. I. "Electron-Phonon Coupling and Spin Fluctuations in the Ising Superconductor NbSe2." Npj Comput. Mater., 9 (1), 1–9 (2023). doi:10.1038/s41524-023-01017-4.
- [31] Wickramaratne, D., Khmelevskyi, S., Agterberg, D. F., Mazin, I. "Ising Superconductivity and Magnetism in NbSe₂." Phys. Rev. X, 10 (4), 041003 (2020). doi:

- 10.1103/PhysRevX.10.041003.
- [32] Hörhold, S., Graf, J., Marganska, M., Grifoni, M. "Two-bands Ising superconductivity from Coulomb interactions in monolayer NbSe₂." 2D Mater., 10 (2), 025008 (2023). doi:10.1088/2053-1583/acb21d.
- [33] Roy, S., Kreisel, A., Andersen, B. M., Mukherjee, S. "Unconventional Pairing in Ising Superconductors: Application to Monolayer NbSe2." 2D Mater., 12 (1), 015004 (2024). doi:10.1088/2053-1583/ad7b53.
- [34] Hybertsen, M. S., Louie, S. G. "Electron Correlation in Semiconductors and Insulators: Band Gaps and Quasiparticle Energies." *Phys. Rev. B*, 34 (8), 5390–5413 (1986). doi:10.1103/PhysRevB.34.5390.
- [35] Rohlfing, M. "Electron-Hole Excitations and Optical Spectra from First Principles." Phys. Rev. B, 62 (8), 4927–4944 (2000). doi:10.1103/PhysRevB.62.4927.
- [36] Roldán, R., Cappelluti, E., Guinea, F. "Interactions and superconductivity in heavily doped MoS₂." Phys. Rev. B, 88 (5), 054515 (2013). doi:10.1103/PhysRevB.88.054515.
- [37] Liu, G.-B., Shan, W.-Y., Yao, Y., Yao, W., Xiao, D. "Three-Band Tight-Binding Model for Monolayers of Group-VIB Transition Metal Dichalcogenides." Phys. Rev. B, 88 (8), 085433 (2013). doi: 10.1103/PhysRevB.88.085433.
- [38] He, W.-Y., Zhou, B. T., He, J. J., Yuan, N. F. Q., Zhang, T., Law, K. T. "Magnetic Field Driven Nodal Topological Superconductivity in Monolayer Transition Metal Dichalcogenides." Commun. Phys., 1 (1), 40 (2018). doi: 10.1038/s42005-018-0041-4.
- [39] Kim, S., Son, Y.-W. "Quasiparticle energy bands and Fermi surfaces of monolayer NbSe₂." *Phys. Rev. B*, 96 (15), 155439 (2017). doi: 10.1103/PhysRevB.96.155439.
- [40] Perali, A., Castellani, C., Di Castro, C., Grilli, M., Piegari, E., Varlamov, A. A. "Two-Gap Model for Underdoped Cuprate Superconductors." *Phys. Rev. B*, 62 (14), R9295–R9298 (2000). doi:10.1103/PhysRevB.62.R9295.
- [41] Maiti, S., Chubukov, A. V. "Superconductivity from Repulsive Interaction." In AIP Conf. Proc., vol. 1550, 3–73 (2013). doi:10.1063/1.4818400.
- [42] Shaffer, D., Burnell, F. J., Fernandes, R. M. "Weak-Coupling Theory of Pair Density Wave Instabilities in Transition Metal Dichalcogenides." Phys. Rev. B, 107 (22), 224516 (2023). doi: 10.1103/PhysRevB.107.224516.
- [43] Haniš, J., Milivojević, M., Gmitra, M. "Distinguishing nodal and nonunitary superconductivity in quasiparticle interference of an Ising superconductor with Rashba spin-orbit coupling: The example of NbSe₂." *Phys. Rev. B*, 110 (10), 104502 (2024). doi: 10.1103/PhysRevB.110.104502.
- [44] Tersoff, J. "Theory and Application for the Scanning Tunneling Microscope." Phys. Rev. Lett., 50 (25), 1998– 2001 (1983). doi:10.1103/PhysRevLett.50.1998.
- [45] Vaňo, V., Ganguli, S. C., Amini, M., Yan, L., Khosravian, M., Chen, G., Kezilebieke, S., Lado, J. L., Liljeroth, P. "Evidence of Nodal Superconductivity in Monolayer 1H-TaS₂ with Hidden Order Fluctuations." Adv. Mat., 35 (45), 2305409 (2023). doi:10.1002/adma.202305409.
- [46] Hamill, A., Heischmidt, B., Sohn, E., Shaffer, D., Tsai, K.-T., Zhang, X., Xi, X., Suslov, A., Berger, H., Forró, L., Burnell, F. J., Shan, J., Mak, K. F., Fernandes, R. M., Wang, K., Pribiag, V. S. "Two-Fold Symmetric Superconductivity in Few-Layer NbSe2." Nat. Phys., 17 (8).

- 949-954 (2021). doi:10.1038/s41567-021-01219-x.
- [47] Nag, P. K., Scott, K., de Carvalho, V. S., Byland, J. K., Yang, X., Walker, M., Greenberg, A. G., Klavins, P., Miranda, E., Gozar, A., Taufour, V., Fernandes, R. M., da Silva Neto, E. H. "Highly Anisotropic Superconducting Gap near the Nematic Quantum Critical Point of FeSelxSx." Nat. Phys., 1–8 (2024). doi:10.1038/s41567-024-02683-x.
- [48] Hutchinson, J., Marsiglio, F. "Mixed Temperature-Dependent Order Parameters in the Extended Hubbard Model." *J. Phys.: Condens. Matter*, 33 (6), 065603 (2021). doi:10.1088/1361-648X/abc801.
- [49] Rubio-Verdú, C., García-García, A. M., Ryu, H., Choi, D.-J., Zaldívar, J., Tang, S., Fan, B., Shen, Z.-X., Mo, S.-K., Pascual, J. I., Ugeda, M. M. "Visualization of Multifractal Superconductivity in a Two-Dimensional Transition Metal Dichalcogenide in the Weak-Disorder Regime." Nano Lett., 20 (7), 5111–5118 (2020). doi: 10.1021/acs.nanolett.0c01288.
- [50] Horcas, I., Fernández, R., Gómez-Rodríguez, J. M., Colchero, J., Gómez-Herrero, J., Baro, A. M. "WSXM: A Software for Scanning Probe Microscopy and a Tool for Nanotechnology." Rev. Sci. Instrum., 78 (1), 013705 (2007). doi:10.1063/1.2432410.